PAPER

Check for updates

Insights into the physicochemical interactions of ionic liquid-coated polymeric nanoparticles with red blood cells†

Christine M. Hamadani, [ID] George R. Taylor, Amber Cecil, Claylee M. Chism, Emilia Huff, Gaya Dasanayake, [ID] Jaylon Everett, Amandeep Kaur, George W. Monroe, Mira Patel, Elisa Pierpaoli and Eden E. L. Tanner [ID] *

Organ-targeted intravenous (IV) delivery of polymeric nanoparticles (NPs) remains a translational drug delivery challenge, as an overwhelming fraction of the administered dose is typically cleared due to fouling at the nano-bio interface. As a solution, we have developed choline carboxylate ionic liquid (IL)-coated polymeric nanoparticles (IL-NPs) that are able to bypass this mechanism of clearance by exhibiting affinity to red blood cells (RBCs) in whole blood, resulting in significant *in vivo* targeted delivery to the first capillary bed encountered post-IV injection in both mice and rats. Here, we demonstrate that choline carboxylate ionic liquid-coated polymeric nanoparticles exhibit *in situ ex vivo* affinity to mouse and human red blood cell membranes in whole blood, and examine the mechanism of action engaged by IL-NPs at the RBC membrane interface. We report the physicochemical impact of varying the anionic alkyl chain structure in choline-based carboxylate ILs, which interfaces on the outermost layer of the NP coating, and reveal that membrane saturation, temperature dependence, and membrane anion transporters all play a role in *in situ* RBC hitchhiking by IL-NPs.

1 Introduction

1.1 The role of anion structure in red blood cell (RBC) hitchhiking engaged by IL-NPs *in situ*

While intravenous (IV) nanoparticle (NP) administration offers promise of biocompatible and organ-targeted drug delivery, polymeric nanomedicines are still hindered in clinical translation due to challenges in specificity and efficacy, which primarily occur from the abundance of undesired interactions with immunological components at the nano-bio interface.[1–4] *In situ* red blood cell (RBC) hitchhiking is a recent therapeutic approach to overcome obstacles such as serum protein opsonization and hepatic clearance in whole blood circulation.[5–7] By physically delivering membrane-attached nanocarriers from the bloodstream to organs *via* capillary shear, drug delivery to desired tissues can be dramatically magnified while avoiding off-target organ accumulation and bloodstream interactions.[8–11] However, understanding the precise mechanism of interaction at the NP : RBC interface, and complex physicochemical dynamics between NPs and carrier RBCs, is still an active area of investigation to develop design principles for *in situ* RBC hitchhiking.[12]

Department of Chemistry & Biochemistry, The University of Mississippi, University, MS 38677, USA. E-mail: eetanner@olemiss.edu; Tel: +1-662-915-1165

† Electronic supplementary information (ESI) available. See DOI: https://doi.org/10.1039/d5na00233h

Ionic liquids (ILs) are composed of bulky asymmetric cations and anions that form liquid salts under 100 °C, and have emerged as a biomaterial class that can be structurally tuned to overcome biological barriers for efficacious and biocompatible drug delivery.[13,14] To this end, we have shown that bioinspired and bio-derived ILs can self-assemble onto the surface of polymeric nanoparticles as either flexibly packed grafts or layer-driven coatings (IL-NPs) to enable highly efficient intravenous nanoparticle delivery *via in situ* RBC hitchhiking.[15–18] In particular, IL choline *trans*-2-hexenoate (CA2HA 1 : 2) coats carboxylic acid-terminated poly (lactic-*co*-glycolic) (PLGA) NPs, *via* cation-mediated electrostatics to the carboxylic-acid PLGA interface, and anion-mediated hydrogen bonding to the cation molecules packed into the coating bulk,[19] such that the outermost interfacing coating layer is comprised of anion molecules, which drive both serum protein repulsion as well as affinity to RBC membranes *in vivo*.[20] This functionality extends IL-NP pharmacokinetic circulation half-life and drives biodistribution to the first capillary bed encountered post-IV injection site in both adult mice and rats.[20,21]

Understanding how ILs modulate NP – blood component interactions in whole blood informs the engineering of next-generation structures to drive targeted NP drug delivery *in vivo*. As such, to build on this work and understand the anion's structural role in the mechanism of RBC hitchhiking by IL-NPs *in situ*, we previously screened a library of 60+ choline carboxylate ILs by structurally engineering the anion around 2HA,
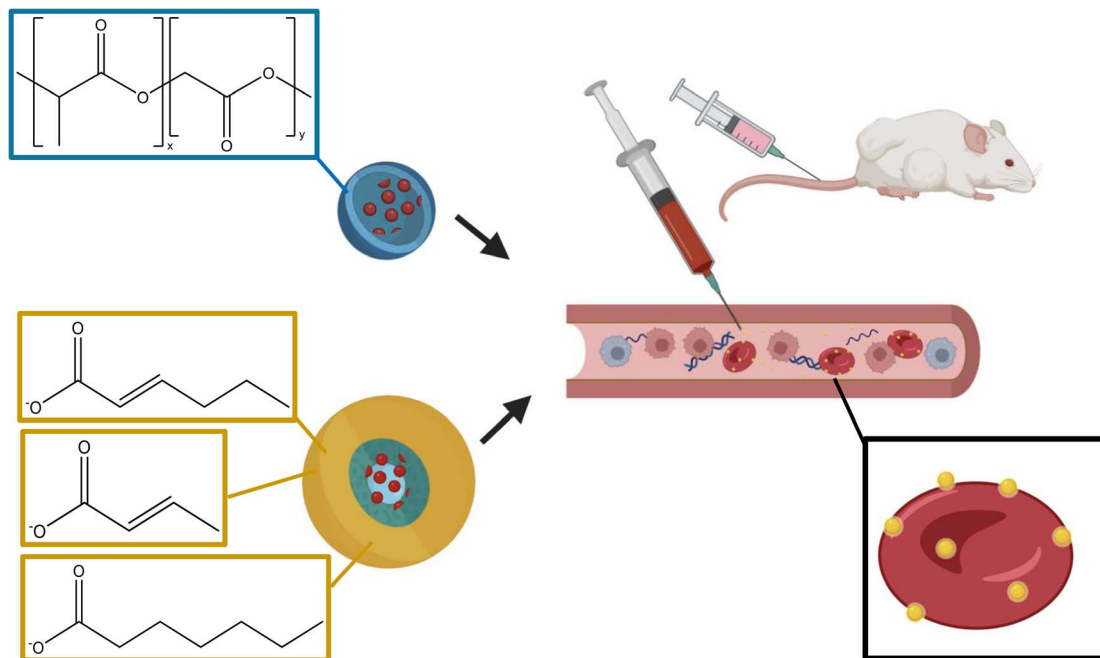
Scheme 1 IL-coated PLGA NPs containing a far-red dye can be used to hitchhike red blood cells (RBCs) *in situ*, as a solution to drive better targeted therapeutic outcomes *in vivo*.

revealing 2 new RBC hitchhiking candidates, choline *trans*-2-butenoate (CA2BE 1 : 1), and choline heptanoate (CAHPA 1 : 1) (Scheme 1).[22]

Here, we use CA2BE 1 : 1 and CAHPA 1 : 1 to explore the physicochemical dynamics governing CA2HA 1 : 2-coated PLGA NP attachment to mouse and human RBCs *in situ ex vivo*, through NP : whole blood dosing, reaction temperature/time dependence, and RBC membrane anion transport inhibition studies.

2   Nanoformulation & characterization of IL–PLGA NPs for *in situ* RBC hitchhiking

To first establish the membrane saturation limit of IL–NP attachment onto RBCs, ILs were synthesized *via* a salt metathesis reaction and bare (uncoated) or IL–NPs were then synthesized *via* nanoprecipitation and solvent evaporation as previously described,[15] incorporating the fluorescent far-red dye 1,1′-dioctadecyl-3,3,3′,3′-tetramethylindocarbocyanine, 4-chlorobenzenesulfonate (DiD) for bio-tracking in whole blood.[22] To verify IL–NP assembly, neat CA2HA 1 : 2, CA2BE 1 : 1, and CAHPA 1 : 1 ILs and their respective IL-coated PLGA NP counterparts were then characterized by Nuclear Magnetic Resonance Spectroscopy (^{1}H NMR, full characterization in Table S1†) and Dynamic Light Scattering (DLS, full characterization in Table S2†). As shown in Fig. 1 below, both cationic and anionic counterparts of the IL assemble onto the carboxylic-acid terminated PLGA surface (67.1 ± 9.3 nm), reflected in the monodisperse (PDI < 0.2) nanoparticle size shift by all three IL-NP candidates (CA2HA: 151.0 ± 19.6 nm; CA2BE: 128.0 ±

26.9 nm; CAHPA: 166.6 ± 37.1 nm) upon coating by DLS. However, the outermost layer of the coating directing interactions with the biological environment is dominated by the anion (which is likely orthogonally oriented in its layer packing[18,19]) and observed by an anionic surface charge shift by all three IL-NP candidates (CA2HA: −51.6 ± 3.4 mV; CA2BE: −55.4 ± 6.9 mV; CAHPA: −53.0 ± 4.8 mV) compared to bare PLGA NP (−30.7 ± 10.3 mV).

3   All IL-NPs reach a limit of RBC membrane saturation in mouse and human whole blood

Bare NPs or IL-NPs in saline buffer were then rotary incubated for 20 minutes at 37 °C with mouse (at 1 mg mL^{-1} NPs) or human gender-pooled whole blood (at 0.5 mg mL^{-1} NPs) at ratios ranging from ~50 NPs : RBC – 980 NPs : RBC (Scheme 2), before isolating and washing RBCs to remove unbound NPs. Interestingly, % DiD+ colocalized RBC singlets (by fluorescence activated cell sorting (FACS, (Fig. 2A and B))) (broadly supported by % NP dose bound to RBCs (by fluorescence plate reader, (Fig. 2C and D))) suggested that CA2HA 1 : 2-coated DiD NPs reached RBC membrane saturation at 218 NPs : RBC (218 *vs.* 890 NPs : RBC, $p = 0.1$, ANOVA and *post hoc* Tukey multi-comparisons test), while CAHPA 1 : 1 (654 *vs.* 890 NPs : RBC, $p = 0.8$) and CA2BE 1 : 1 (654 *vs.* 890 NPs : RBC, $p = 0.6$) both reached RBC membrane saturation at 654 NPs : RBC in mouse whole blood despite increasing NP: whole blood dose (Fig. 2). In human whole blood, CAHPA 1 : 1 and CA2BE 1 : 1 both reached saturation at 218 NPs : RBC (218 *vs.* 890 NPs : RBC, $p = 0.9$), while CA2HA 1 : 2 conserved membrane saturation at 218 NPs : RBC
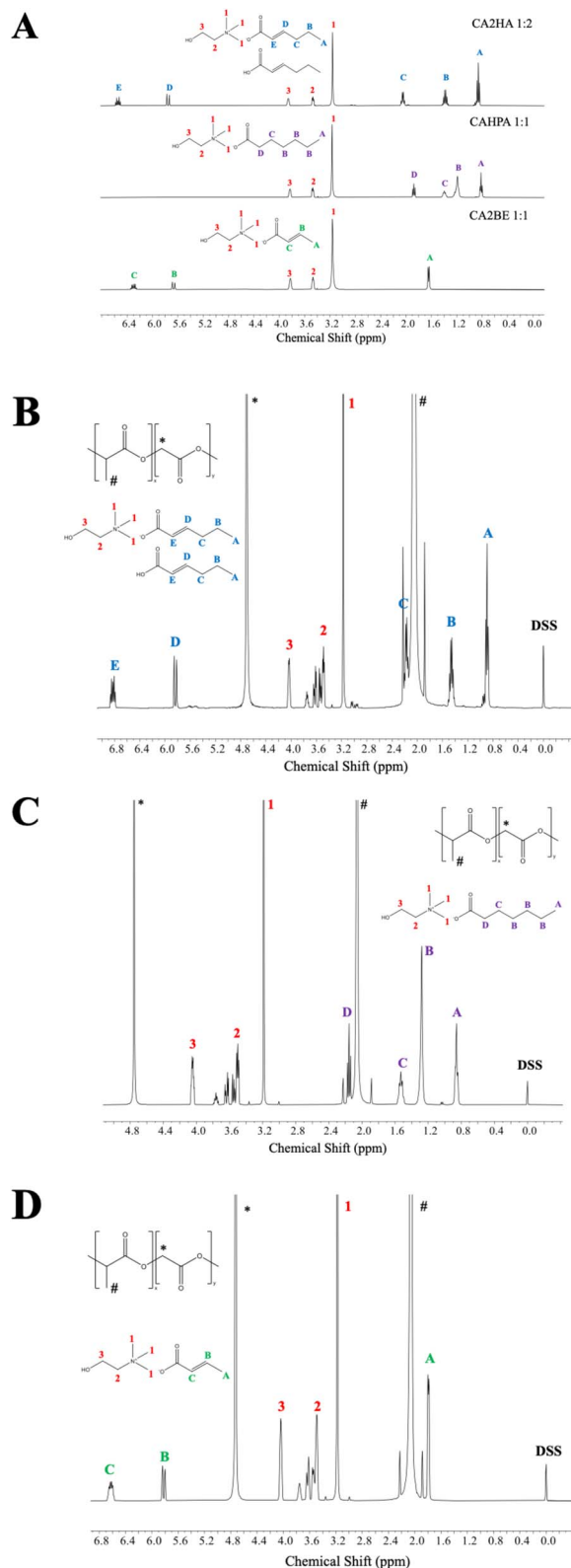
Fig. 1 ^{1}H NMR spectroscopy confirms assembly of both anionic and cationic components onto PLGA NPs. (A) Neat IL NMR profiles of CA2HA 1 : 2, CAHPA 1 : 1, and CA2BE 1 : 1 at 400 MHz in DMSO-d$_6$. (B) CA2HA 1 : 2-coated PLGA NP profile in D$_2$O (1 mg), (C) CAHPA 1 : 1-coated PLGA NP profile in D$_2$O (1 mg), (D) CA2BE 1 : 1-coated PLGA NP profile in D$_2$O (1 mg).

(218 *vs.* 890 NPs : RBC, $p = 0.2$). This difference suggests different membrane components at the RBC interface that may be responsive to docking by CA2HA *vs.* CAHPA and CA2BE, and that affinity to that membrane composition may vary between species.

In contrast, RBC binding engaged by bare NPs was significantly lower than all 3 IL-NP candidates at every dosing condition ($p < 0.01$, ANOVA with *post hoc* Tukey) (Fig. 2A and B). While bare PLGA NP binding proportionally increased with dose in whole mouse blood ($p < 0.01$ at 980 NPs : RBC *vs.* all 3 IL candidates), it remained much lower and more subtle in human whole blood (under 0.5% by FACS and under 3% by plate reader at 980 NPs : RBC. This observed species difference for bare NPs reflects the harsher immunogenic landscape in human whole blood (needing to overcome plasma protein adsorption and white blood cell phagocytosis),[23,24] while the difference observed between coated and uncoated NPs suggests a difference in chemical *vs.* physical binding, whereby IL-NPs have a specific affinity to the membrane that can reach a threshold as opposed to noncovalent attachment.[25,26]

4 Anion identity impacts the temperature dependence of IL-NP binding to RBCs *in situ*

To investigate how anion identity impacts temperature-dependence of IL-NP binding over time in whole blood, bare or IL-coated DiD NPs in saline buffer were again rotary incubated with mouse or human gender-pooled whole blood (at a 109 NP : RBC ratio). The samples were mixed at either 37 °C or 4 °C (in a cold room), for a total mixing time of between 2–120 minutes. When isolated RBCs were examined again for colocalized NP fluorescence by FACS (Fig. 3), both species type and anion identity were observed to play a strong role in IL-NP binding in response to temperature of mixing.

At 20 minutes of incubation with BALB/c whole mouse blood, binding engaged by bare PLGA NPs reduced 5-fold at 4 °C compared to 37 °C, while temperature change had no impact in human blood. For BALB/c whole blood treated by bare PLGA NPs, the effect of transitioning the temperature of incubation from 37 °C to 4 °C was not statistically significant at earlier timepoints; however, longer times of rotary incubation were impacted by temperature (16–20 minutes: $p < 0.05$, 45–120 minutes: $p < 0.01$, Table S3†). This outcome is unlikely to be a specific relationship between the PLGA NP and the membrane, and rather may result in part due to the lack of kinetic energy at 4 °C necessary to drive mechanical interactions (such as noncovalent adsorption and van der Waals's interactions) as the NPs reversibly engaged with the RBCs despite the overall increasing binding trend over time.

In comparison, the order of IL-NP temperature sensitivity depended on both anion structure and species. In mouse blood, RBC binding by CAHPA 1 : 1 was the most sensitive (11× reduction from 37 °C to 4 °C), while binding by CA2HA 1 : 2 reduced 9×, and RBC hitchhiking by CA2BE 1 : 1 was the least sensitive to temperature decrease (reduced 4.7×) compared to
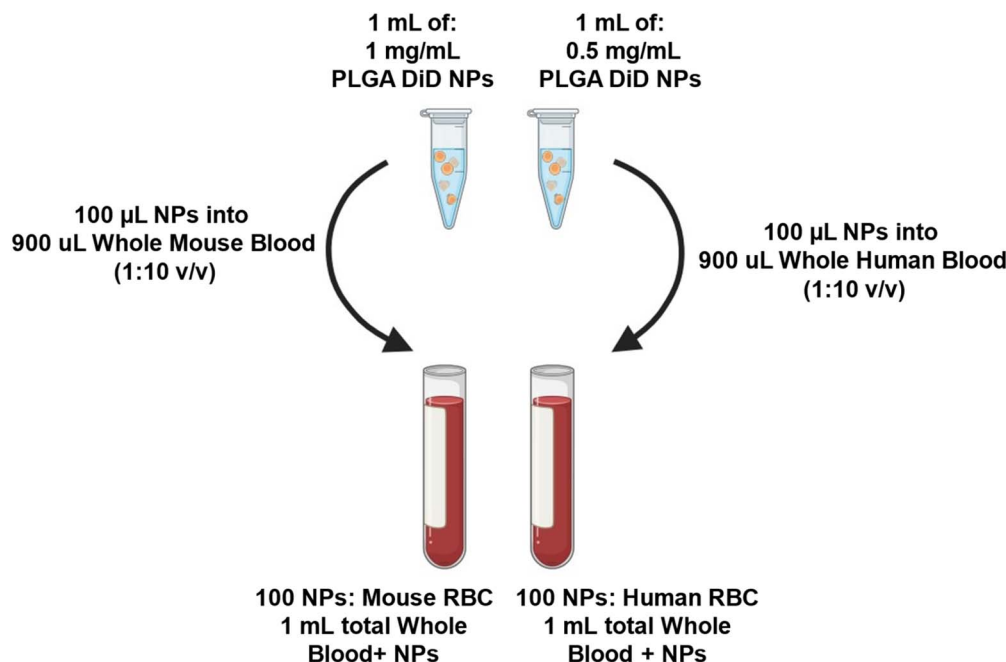
Scheme 2 Administration scheme of DiD NPs into human and mouse whole blood to constitute ~100 : 1 NP : RBC ratio. Figure created in and adapted from BioRender.

binding at 37 °C. In human whole blood, CA2HA 1 : 2 showed a ~36-fold RBC binding reduction, CAHPA 1 : 1 reduced 4.3×, and CA2BE 1 : 1 demonstrated the least temperature sensitivity

(1.7× reduction relative to 37 °C). The difference in this order may be partially contributed to by the flexibility of the anion's alkyl tail length,[27] where necessary phospholipid reorganization
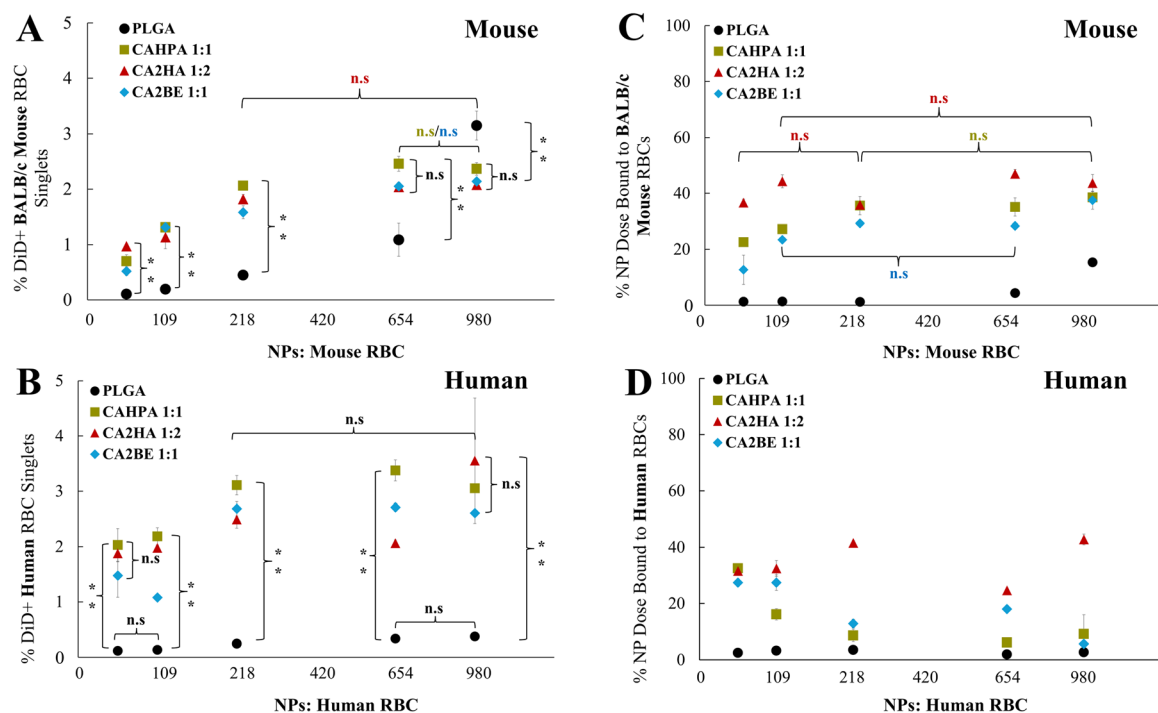

Fig. 2 All IL-NPs reach a limit of RBC membrane saturation when dosing mouse and human whole blood from ~50 NPs : RBC – 980 NPs : RBC ratios. FACS demonstrates % RBC singlets colocalized with DiD NPs after dosing (A) BALB/c mouse gender-pooled mouse whole blood, or (B) human gender-pooled whole blood. Fluorescent plate reader demonstrates % NP fraction present on isolated RBCs after dosing (C) BALB/c gender-pooled mouse whole blood, or (D) human gender-pooled whole blood. All raw data is subtracted by saline buffer-treated controls and represented as an average of $n = 3$ biological repetition ± standard deviation. Multi-comparison statistics were performed using an ANOVA with *post hoc* Tukey, where * = $p < 0.05$, ** = $p < 0.01$, *** = $p < 0.001$.
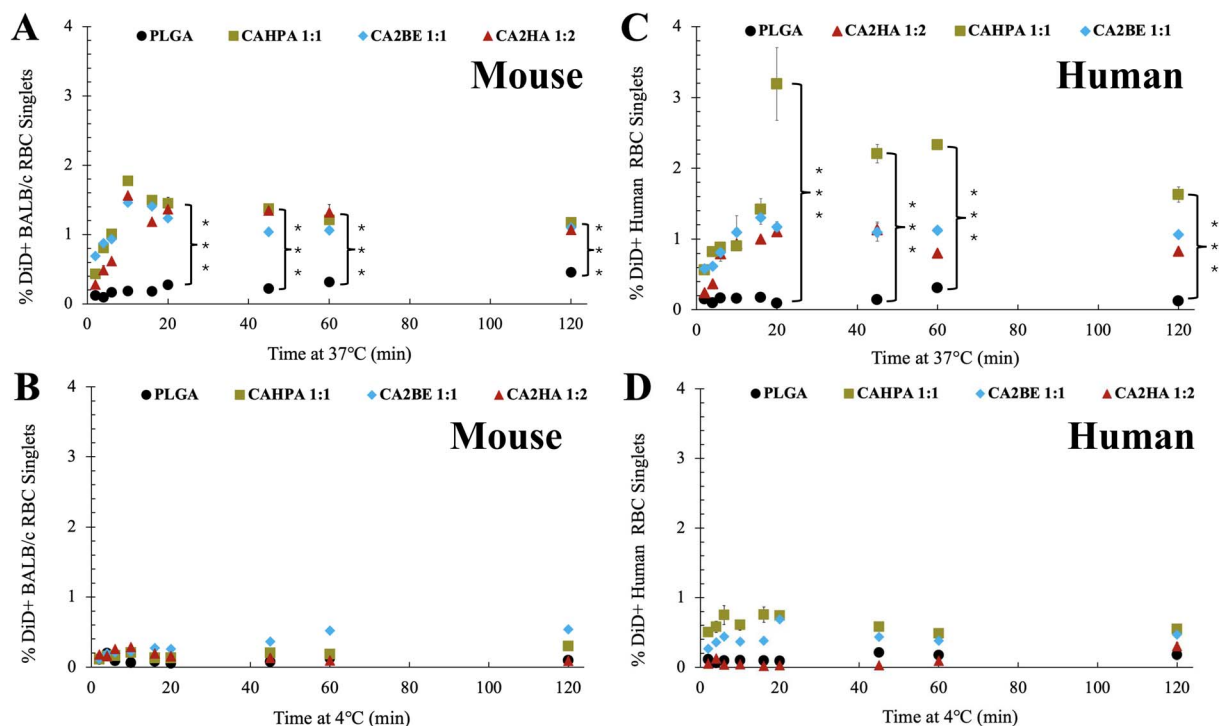
Fig. 3 Anion identity impacts the temperature dependence of IL-NP binding over time to mouse and human RBCs in whole blood transitioning from (A & C) 37 °C to (B & D) 4 °C. FACS of DiD-colocalized (A) BALB/c RBC singlets after 2–120 minutes of mixing at 37 °C; 2–10 min linear trend R^2 values for HPA: 0.99, 2BE: 0.96, 2HA: 0.94, (B) BALB/c RBC singlets after 2–120 minutes of mixing at 4 °C, (C) human RBC singlets after 2–120 minutes of mixing at 37 °C; 2–16 min log trend R^2 values for HPA: 0.83, 2BE: 0.91, 2HA: 0.91, and (D) human RBC singlets after 2–120 minutes of mixing at 4 °C. All raw data is subtracted by saline buffer-treated controls and represented as an average of $n = 3$ biological repetition ± standard deviation. Statistics is represented as an ANOVA with *post hoc* Tukey conducted on 4 samples at a time, where * = $p < 0.05$, ** = $p < 0.01$, *** = $p < 0.001$.

or fluidization during insertion at the lipid-cell membrane interface[18,28,29] is not as efficient at cold temperatures due to factors such as matrix conformational distortion and stiffness in RBC deformability,[30–33] resulting in the longest chain anions (HPA and 2HA) demonstrating the highest temperature sensitivity and the shortest anion (2BE) demonstrating the least temperature sensitivity.

When examining the dynamics of mouse and human RBC binding in whole blood over time under physiological conditions, all 3 IL-NPs consistently outperformed bare NPs (ANOVA, $p < 0.001$). Bare PLGA NPs overall demonstrated a similar curve profile at every time point, with its highest performing condition under 0.5% after 120 minutes of rotary incubation at 37 °C (and 2.5× less than all 3 IL-NPs at that condition). Notably, regardless of structure, all 3 anions (HPA, 2HA, and 2BE) demonstrated an initial mouse RBC binding increase (with a linear-leaning trend) from 2–10 minutes, with a decrease from 10–16 minutes, followed by a plateau from 20–120 minutes. For human RBCs, an initial binding increase (with a logarithmic-leaning trend) was instead observed from 2–16 minutes before the plateau, likely due to species differences in both RBC size and membrane composition.[34] This may suggest a potential two-phase kinetic binding profile where the IL-NPs reversibly dock onto RBCs by way of either a receptor or noncovalent lipid

interaction, before establishing an irreversible chemical interaction at the membrane interface.[35]

5 Varying anion structure drives docking affinity to different RBC membrane transporters

To understand specifically which aspect of the RBC membrane is responsible for the docking of IL-NPs in whole blood, we rationalized that anion transporters, such as monocarboxylate transporter 1 (MCT1) and anion exchanger 1 (AE1/band 3), may play a role due to their nature in transporting and exchanging short and medium chain carboxylate anions as well as weak acids, much like the anions 2BE, 2HA, and HPA.[36–38] Specifically, we hypothesized there may be a correlation between IL-NP membrane saturation, the observed dynamic behavior of IL-NP binding over time, and the similar differences in temperature sensitivity and resulting kinetics engaged by MCT1 and AE1.[39–41]

To examine this, we closely adapted anion transporter inhibition protocols from prior studies[21,42] to test the binding capacity of bare or IL-NPs on freshly isolated mouse or human RBCs pre-treated with specific anion transport inhibitors. We rationalized that if the IL-coated NPs were docking at sites of anion transport at the RBC membrane interface, then pre-
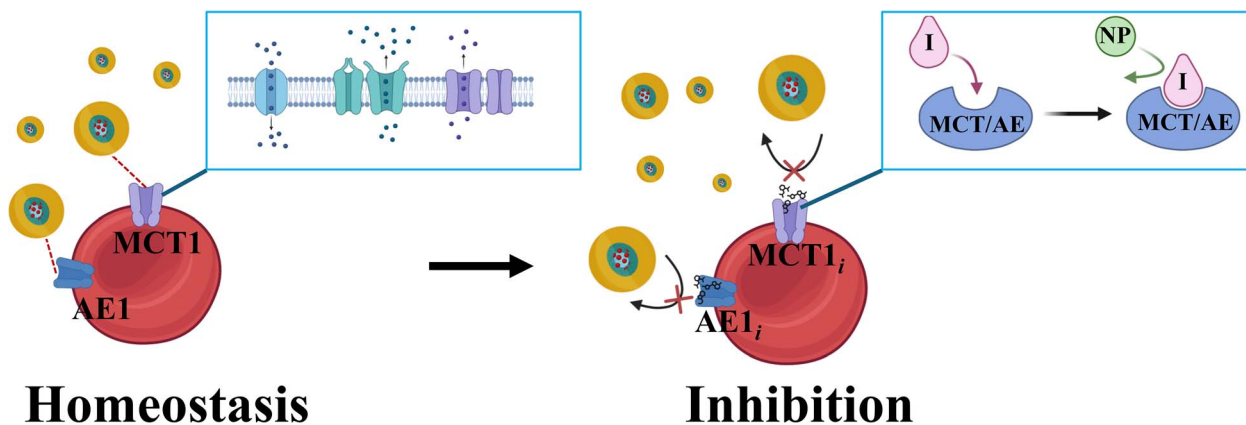
Scheme 3 Specific anion transport inhibitors obstruct active sites at the outwards-facing interfacing sites of monocarboxylate transporter 1 (MCT1) or anion exchanger 1 (AE1) at the RBC membrane with high affinity, blocking the alkyl tail chain present in the outermost anion layer of the IL coating (gold) from establishing an initial docking site to allow binding to the membrane. Key: I (Inhibitor), NP (Nanoparticle), $AE1_i$ and $MCT1_i$ refer to the inhibited versions of the anion transporters. Figure created and adapted from BioRender.

treatment with inhibitor would block this docking phenomena and accumulate more NPs in the first wash, hence decreasing the quantity of NPs bound to the RBCs (shown below in Scheme 3).

To perform this experiment, mouse or human RBCs were isolated and washed from gender-pooled fresh whole blood and subsequently treated (as described in Methods and materials,

and optimization shown in Fig. S1†) with MCT1 inhibitor (10 µM AR-C1558858, which specifically inhibits transmembrane helices 7–10),[42] AE1 inhibitor (1 µM 4,4′-diisothiocyanatos-tilbene-2,2′-disulfonate (DIDS), which reduces anion affinity by covalently binding to transmembrane 13's residues K539 and K851),[43] GLUT1-4 control inhibitor (100 µM phloretin, PHL)[44] or no inhibitor (pre-treated with 0.9% saline, or DMSO control).
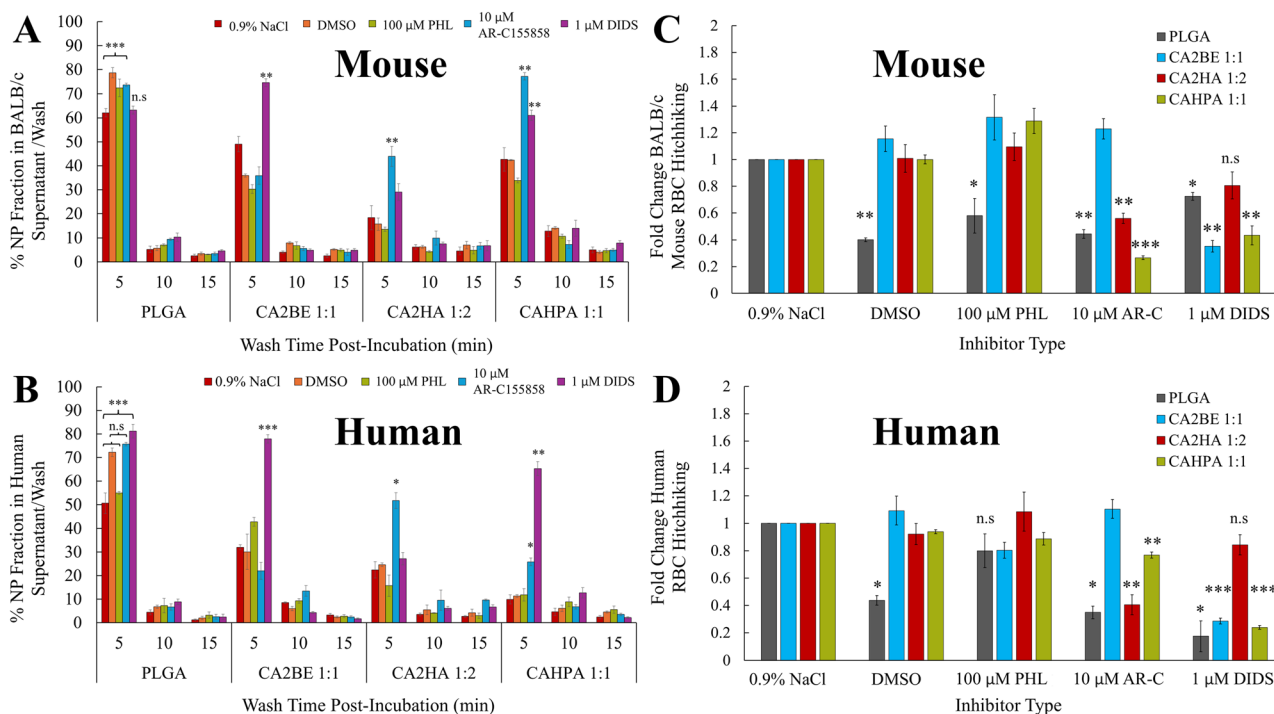

Fig. 4 Anion structure drives docking affinity to different species-dependent RBC membrane transporters. Data is represented % DiD NP dose (1032 NPs: human or mouse RBC), detected by fluorescent plate reader, in the supernatant each wash and final washed cell pellet, in response to inhibitor or controls for hitchhiked (A & C) mouse RBCs or (B & D) human RBCs. (C & D) Cell pellet data for every inhibitor pre-treatment condition is additionally normalized as fold-change of bare or IL-NP binding compared to uninhibited saline pre-treated RBCs, such that each inhibitor or control (DMSO) induced either fold-gain or fold-loss in NP binding capability to the RBC membrane. Data is represented as $n = 3$ biological repetition ± standard deviation. Statistics is represented as paired two-tailed t-test of means conducted on two samples at a time or ANOVA with *post hoc* Tukey for three or more samples at a time, where * = $p < 0.05$, ** = $p < 0.01$, *** = $p \leq 0.001$.

Paper

View Article Online

Nanoscale Advances

The GLUT transporter was chosen as a control inhibitor for potential damage to the RBC membrane as a result of general inhibition, and to distinguish the impact of inhibiting anion *vs.* non-anion transporters. After mouse and human RBCs were incubated with inhibitor and treated with Bare or IL-coated DiD NPs, RBCs were washed 3 times to remove unbound NPs, with the hypothesis that the weakest bound NPs would emerge into the supernatant in the first wash, and consequently the strongest bound NPs would be present in the third wash. As such, the supernatant was collected during each wash, along with the final cell pellet, and DiD fluorescence of each fraction was measured by fluorescent plate reader (Fig. 4). We additionally performed a control hemolysis assay under the same conditions that demonstrated that IL-NPs alone did not induce RBC membrane damage at the same NP : RBC treatment condition in the absence of inhibitor (Fig. S2†).

Compared to human RBCs treated with 0.9% saline, all inhibition agents with the exception of GLUT ($p = 0.29$, *post hoc* Tukey HSD) caused bare PLGA NPs to readily accumulate into the supernatant of the first wash ($p = 1.0 \times 10^{-7}$ by ANOVA, denoted as '5 minutes' in Fig. 4A and B). For BALB/c mouse RBCs, bare PLGA NPs demonstrated a similar accumulation profile in the supernatant of wash 1 ($p = 1.1 \times 10^{-5}$, ANOVA) with sensitivity to all inhibitor agents ($p = 0.001$, Tukey HSD) except DIDS Anion Exchanger 1 inhibitor ($p = 0.9$, Tukey HSD). As such, PLGA's varying sensitivity to different membrane transport inhibitors across BALB/c and human RBCs highlights the importance in considering species-dependent membrane composition in RBC hitchhiking by NPs. However, the disruption of RBC binding by PLGA NPs was significantly and dominantly affected by DMSO solvent alone in both mice and humans ($p = 0.001$, *post hoc* Tukey HSD). As the RBC stocks were treated with a comparable volume of DMSO control as inhibitors in DMSO, the effect of the inhibitor itself appears non-specific for PLGA NPs and may be attributed to the solvent used, which is reflected by PLGA's significant and non-specific reduction response in RBC binding (Fig. 4C and D). In this case, DMSO may likely interfere with non-covalent forces and solvation interfaces between PLGA NPs and the RBC membrane required during mechanical interaction, which would occur much less frequently and less strongly in a competitive whole blood environment.

In contrast, compared to uninhibited saline control (0.9% NaCl) for mouse RBCs, NP : RBC binding enabled by CA2HA 1 : 2 was significantly and selectively diminished by MCT1 inhibitor AR-C155858 ($p = 0.003$) while GLUT ($p = 0.3$), DMSO control ($p = 0.9$), and AE1 inhibition ($p = 0.08$) had no impact. MCT1 inhibition also induced the most DiD NP accumulation in the supernatant for CA2HA 1 : 2 post-wash 1 ($p = 0.001$). This selective outcome by MCT1 inhibition was also observed in human RBCs for both supernatant NP detection in wash 1 ($p = 0.01$) and NP binding reduction in the cell pellet ($p = 0.005$). In contrast, CAHPA 1 : 1-mediated NP binding in mouse RBCs was equally affected by AE1 (wash 1; $p = 0.009$, cell pellet; $p = 0.005$) as well as by MCT1 (wash 1; $p = 0.004$, cell pellet; $p = 0.0001$) inhibition, which was also reflected for human RBCs as well, although AE1 inhibition was slightly more efficacious (wash 1; p

$= 0.003$, cell pellet; $p = 0.0001$) than MCT1 inhibition (wash 1; $p = 0.02$, cell pellet; $p = 0.003$).

Notably, the structural anion shortening of *trans*-2-hexenoate (2HA) to *trans*-2-butenoate (2BE) resulted in a strong pivot in selective IL-NP affinity to the AE1 transporter at the cell membrane interface for both mouse (wash 1; $p = 0.007$, cell pellet; $p = 0.001$) and human (wash 1; $p = 8 \times 10^{-5}$, cell pellet; $p = 0.0003$) RBCs, with some additional participation between the 2BE anion and the GLUT transporter in human RBCs. While this result is not significant, structural analogs of 2BE are able to translocate GLUT on cell membranes, which may suggest additional potential 2BE: GLUT interaction on RBCs.[45] When considering the performance of all three anions in response to AE1 or MCT1 inhibition, the explanation for the correlated shift in anion structure and anion transporter affinity may be contributed to by several simultaneous events.

Firstly, the specific interaction of AR-C155858 into transmembrane helices 7–10 and 2HA's selective response to MCT1 inhibition may suggest alkyl tail docking within that domain to transition the IL-NP into its irreversible binding phase throughout 20–120 minutes of rotary incubation in whole blood.[46] However, when the alkyl tail chain length is extended and more flexible in HPA, its anion transport affinity becomes more promiscuous and may be able to additionally interface with AE1 at transmembrane 13 or coordinate into elongated transmembrane 11 and intracellular loop 5.[47] Unexpectedly, 2BE transport (also known as crotonic acid) is unresponsive to MCT1 inhibition on RBCs, which has been well established as a traditional crotonate cell uptake route.[48] Instead, 2BE is strongly and selectively inhibited by DIDS, suggesting that it may be covalently inserting itself into AE1 through transmembrane residue K851 *via* lysine crotonylation in a two-step binding mechanism.[49–51]

6 Conclusions

We thus report here that, depending on the length and structure of their anionic alkyl tail, choline carboxylate ILs can self-assemble on PLGA NPs to drive RBC hitchhiking *via* specific anion membrane transporters *in situ*, particularly MCT1 for CA2HA 1 : 2, AE1 for CA2BE 1 : 1, and a combination of MCT1 and AE1 for CAHPA 1 : 1 due to its longer flexible tail and saturated chain. Additionally, we demonstrate that despite increasing the IL-NP dose in whole blood, the anion structure of all three ILs reach or approach a limit of NP saturation at the RBC membrane at 218 NPs : RBC in whole blood. Lastly, we demonstrate that the binding dynamics of all three IL-NPs have a similar trend of increase and plateau over 120 minutes of rotary incubation, suggesting a two-phase binding mechanism of reversible docking and irreversible attachment. However, each anion structure had both different and species-dependent sensitivities to reaction temperature, informing membrane favorability as a response to alkyl tail length and flexibility. Overall, our findings highlight the importance of understanding how ILs modulate NP – blood component interactions in whole blood to engineer next-generation structures to drive targeted NP drug delivery *in vivo*.

7 Experimental section/methods

7.1 Materials

For IL synthesis, *trans*-2-hexenoic acid anion, 98% (Sigma-Aldrich, Cat # W316903-1KG-K), *trans*-2-butenoic acid, 98% (113018-500G), and heptanoic acid anion, 96% (146870-100ML), along with choline bicarbonate cation (80% in water) (Sigma-Aldrich, # C7519-500ML), were obtained from Sigma-Aldrich. ^{1}H NMR spectroscopy was performed using a 400 MHz Bruker Ascend. NMR solvents consisted of either DMSO-D_6 (99.96 atom% D) (Sigma-Aldrich, Cat # 156914-10) or D_2O (Sigma-Aldrich, Cat # 151882-500G). A Karl Fischer Metrohm Coulometer (Cat # 899) was used to evaluate water content. For nanoprecipitation, 40 kDa carboxylic-acid terminated poly(D,L-lactide-*co*-glycolide) 50 : 50 (PLGA) was obtained from nanosoft polymers (Cat # 11541-40K-50:50-5 g) and dissolved in HPLC-grade acetonitrile (Sigma-Aldrich, Cat # 34851-4). Hydrophobic far-red dye 1,1′-dioctadecyl-3,3,3′,3′-tetramethylindo-carbocyanine, 4-chlorobenzenesulfonate salt solid (DiD) (ThermoFisher, Cat # D7757) was used to track NPs in whole blood. Sterile filtered cell-culture grade water was obtained from Cytiva (Cat # SH30529.02). Filtration was performed with a Thermo Scientific Sorvall Ultracentrifuge (Cat # ST8R) and 30 kDa MWCO EMD Millipore Amicon Ultra-4 filters (Cat # UFC803024). Internal standard sodium 2,2-dimethyl-2-sila-pentane-5-sulfonate-d_6 (d, 98%) (DSS) was obtained as a 0 ppm NMR control from Cambridge Isotope Laboratories and used at 0.2 mg per tube (Cat # DLM-8206-1). For DLS characterization studies, a Malvern Zetasizer (Pro Blue) was used for DLS measurements along with a zeta potential dip cell (Malvern ZEN1002) and DTS 0012 polystyrene cuvette. Commercial whole mouse and human gender-pooled, donor-pooled blood anti-coagulated with k_2EDTA was obtained from Bio-IVT, USA. Rotary incubation of NPs and blood was performed using a Roto-Therm from Benchmark Scientific, #H2024. Fluorescent quantitative measurements were made using a Greiner Fluo-rotrac black-bottom 300 μL 96-well plate (Greiner Bio-One, Cat # 655076) and Cytation 5 imaging fluorescent plate reader (Agilent technologies, Model CYT5MF), or a Thermo Fisher Scientific Attune Nxt Flow Cytometer. For inhibition experiments, cell-grade DMSO was obtained from Sigma-Aldrich, #D2438-50ML, GLUT inhibitor Phloretin was obtained from Sigma-Aldrich, #P7912-100MG. AE1 inhibitor 4,4′-diisothiocyanatos-tilbene-2,2′-disulfonate (DIDS) was sourced from Sigma-Aldrich, #D3514-100MG, and MCT1 inhibitor AR-C155858 was acquired from Selleck Chemicals, #S7919.

7.2 Ionic liquid synthesis and characterization

Choline *trans*-2-hexenoate (CA2HA 1 : 2), choline *trans*-2-bute-noate (CA2BE 1 : 1), and choline heptanoate (CAHPA 1 : 1) were synthesized as previously published.[22] Briefly, choline bicar-bonate was combined with each anion at its specific ionic molar ratio while stirring in an oil bath at 40 °C. After stirring over-night, each IL was rotary evaporated for 2 hours at 15 mbar and 60 °C, before being vacuum dried for 48 hours at −760 mmHg and 60 °C. The resulting IL product was evaluated for yield,

water content by Karl Fischer titration, density, and for chemical identity by NMR, summarized in Table S1.†

7.3 NP synthesis and characterization

Bare PLGA and IL-PLGA NPs were synthesized and character-ized as previously published in literature.[15,20,21] Briefly, 1 mL of organic phase consisting of fluorescent far-red dye 1,1′-dio-ctadecyl-3,3,3′,3′-tetramethylindocarbocyanine, 4-chlor-obenzenesulfonate (DiD), PLGA, and acetonitrile (1 mg mL^{-1} PLGA, 2%/wt PLGA DiD) was added dropwise in a 20 mL scin-tillation vial of either 3 mL of sterile cell-culture-grade water or D_2O water (for NMR) and stirred on a magnetic stir plate in the dark at 1200 rpm at 25 °C for 3 hours. Neat IL (depending on density, 10–20 mg mg^{-1} PLGA) was then added in the form of a liquid drop to the center of the reaction solution while stirring at 800 rpm and stirred for a total of two more hours (at 800 rpm for 1 h and at 900 rpm for 1 h). Coated IL-NPs were then centrifuge-filtered using a molecular weight cutoff of 30 kDa at 4 °C and 2500 rpm for 1 h, while uncoated PLGA NPs were more gently filtered at 2000 rpm to prevent disruption. The resulting filtered NP concentrates were then resuspended to 1 mg mL^{-1} with D_2O or 0.9% USP injection-grade saline for either charac-terization or biological application and stored up to 2 weeks at 4 °C with light protection although typically used within 48 h post-synthesis. Filtered and resuspended 1 mg mL^{-1} NPs were characterized for size and surface charge by Dynamic Light Scattering (Table S2†) at a 1 : 10 (v/v) dilution in cell-grade water, using a 40 s calibration optimization time and fluorescent filter.

7.4 RBC dosing in whole blood and temperature kinetics of IL-NP binding

Bare PLGA DiD NPs, CA2HA 1 : 2 PLGA DiD NPs, CA2BE 1 : 1 PLGA DiD NPs, and CAHPA 1 : 1 PLGA DiD NPs were evaluated alongside 0.9% saline controls for RBC hitchhiking in whole BALB/c mouse or human gender-pooled whole blood (k_2EDTA anticoagulated). Briefly, for dosing studies, whole mouse or human blood (Bio-IVT, USA) was incubated with DiD NPs at 1 : 20, 1 : 10, 1 : 5, 1 : 2.5, and 1 : 2 (v/v) ratios, which correspond respectively to NP : RBC ratios in whole blood of ∼50 : 1, 109 : 1, 218 : 1, 654 : 1, and 980 : 1. Mouse RBCs are roughly half the size of human RBCs, and are present in double the number in the same volume of whole blood: as such, to ensure that volume dosing ratios were equivalent between species (100 NPs: mouse or human RBC), the concentration of NPs for mouse blood (1 mg mL^{-1}) was adjusted for human blood to 0.5 mg mL^{-1} in 0.9% saline (Scheme 2).

Whole blood treated with NPs or saline was then rotary incubated under standard conditions at 50 rpm (Benchmark Scientific, #H2024) for 20 minutes at 37 °C. For temperature sensitivity studies, whole blood was instead combined with DiD NPs at 109 NPs : RBC and either at 37 °C or at 4 °C in a cold room, for total mixing time endpoints of 2, 4, 6, 10, 16, 20, 45, 60, or 120 minutes. Incubated whole blood at each endpoint (2–120 min) was then centrifuged at 1000×g, 10 min, at 4 °C and RBCs were manually isolated and washed to remove unbound NPs. Briefly, isolated RBCs were resuspended to the original

whole blood volume with saline and washed at $200 \times g$ and 4 °C for 5 min, which was then repeated a total of three times.

Final washed RBC pellets were resuspended to 1 mL, from which 200 µL was again diluted to 2 mL with saline buffer and measured for % DiD+ colocalized RBC singlets using a Thermo Fisher Scientific, Attune Nxt Flow cytometer, or measured quantitatively by fluorescent plate reader for % administered NPs that bound to RBCs. For flow cytometry studies, 100 000 cell events (from 250 µL acquisition volume) were measured at the slowest instrument flow rate (12.5 µL min^{-1}). All events were first gated by scattering to identify singlet RBCs (y-axis: SSC-A, x-axis: FSC-A), which were then gated again to re-validate viable RBC singlets (y-axis: FSC-H, x-axis: FSC-A). The final singlet population was then examined for far-red colocalization using the RL1 laser (y-axis: SSC-A, x-axis: RL1-A). Background noise from saline was to evaluate where to gate DiD colocalization and subtracted from sample measurements.

For fluorescent plate reader (Cytation 5 imaging fluorescent plate reader (Agilent technologies, Model CYT5MF)) measurements (ex. 640, em. 670), dosage experiments were repeated such that a lower volume of whole blood was used, and special care was taken to prevent cell yield-loss during handling, fraction isolation, transfer, or washes. Washed RBCs were resuspended, diluted, and read (at 250 µL per well) on a Greiner Fluorotrac black-bottom 300 µL 96-well plate (Greiner Bio-One, Cat # 655076) at 37 °C. Signals were background subtracted using saline controls, and final RBCs signals were scaled by a factor which depended on the necessary dilution. Treatment statistics on triplicate samples were either performed via ANOVA for 3 or more samples at a time, or via paired two-tailed t-test of means for two samples at a time.

7.5 Anion transport-mediated inhibition of RBC hitchhiking

Anion transport inhibition of BALB/c and human RBCs were performed based on a slight modification to previously published protocols.[21,42] MCT1 and AE1 inhibitors were additionally respectively titrated in BALB/c RBCs to determine optimal inhibitor concentrations (Fig. S2†). First, RBCs were isolated from either commercial BALB/c or human gender-pooled whole blood (Bio-IVT, USA) as described above. After washing the isolated RBCs to remove any traces of hemolytic events or cellular debris, 1 : 50 (v/v) BALB/c RBC stocks were made in 0.9% saline, and to ensure that human RBCs were receiving equivalent inhibitor and NP doses to mouse RBC stocks, 1 : 25 (v/v) human RBC stocks were made in 0.9% saline.

Stocks were then treated at either 100 µM Phloretin (Sigma-Aldrich, #P7912-100MG), 1 µM 4,4′-diisothiocyanatostilbene-2,2′-disulfonate (DIDS) (Sigma-Aldrich, #D3514-100MG), 10 µM AR-C155858 (Selleck Chemicals, #S7919) (all formulated in cell-grade DMSO (Sigma-Aldrich, #D2438-50ML), or controls that consisted of either 0.9% saline (untreated) or an equal amount of DMSO (0.6% (v/v)). Inhibitor-treated RBCs were then rotary incubated for 5 minutes at 5 rpm and 37 °C to evenly mix before incubating in a cell-culture grade incubator for 25 more minutes at 37 °C. After 30 total minutes of incubation at 37 °C, NPs were combined with their respective inhibited stocks in

triplicate, and rotary incubated for 20 minutes at 37 °C and 50 rpm. Washing steps then proceeded as described above (3 washes at $200 \times g$, 5 minutes, 4 °C per wash).

Each supernatant fraction was fully collected and was transferred (at 250 µL per well) to a Greiner Fluorotrac black-bottom 300 µL 96-well plate, such that every wash and the final pellet (which was resuspended to 1 mL with saline) was transferred to the plate in triplicate. In this way, no NP sample nor blood sample was discarded, and could be summed (including a 4× scale factor for signal from the diluted RBC pellet) to generate a total expected fluorescent 'yield' and generate % NP dose/fractions. % NP dose/RBC fraction was reported as fold-change to 0.9% saline (non-inhibited), and statistics were performed via paired two-tailed t-test of means for one sample of interest vs. 0.9% saline at a time.

7.6 Hemocytocompatibility of IL PLGA DiD NPs on isolated mouse and human RBCs

Evaluation of hemolysis after incubation of isolated RBCs with DiD NPs was performed as previously published.[15,20] RBCs were isolated from commercial mouse or human gender pooled whole blood and washed to create 1 : 50 (v/v) (mouse) or 1 : 25 (v/v) (human) RBC stocks as described above in Section 7.5. DiD NPs (PLGA, CA2HA 1 : 2, CAHPA 1 : 1, and CA2BE 1 : 1) were then combined with isolated mouse or human RBCs at NP : RBC ratios of 1032 : 1 (corresponding with the treatment condition in Section 7.5), along with higher NP : RBC concentrations of 2178 : 1 and 4092 : 1. NP-treated RBC samples were then incubated in a cell-culture incubator at 37 °C for 1 hour, and then spun down in an ultracentrifuge at $500 \times g$ for 10 min at 4 °C. 100 µL of the supernatant was then plated in a 96-well clear plate (Nunc) and absorbance was read at 410 nm on a Cytation 5 plate reader. Sample calculations are provided below for estimating NP : RBC dosages.

In 225 µL BALB/c mouse whole blood (WB):

$$10.2 \times 10^6 \text{ RBC per µL WB}$$

$$\Rightarrow 225 \text{ µL WB} \times (10.2 \times 10^6 \text{ RBC per µL WB}) = 2\,295\,000\,000 \text{ RBCs}$$

90 µL collected RBC pellet $\Rightarrow 2\,295\,000\,000$ RBCs in total pellet

In 500 µL stock (1 : 50 v/v):

10 µL pellet taken for 1 : 50 v/v stock $\Rightarrow 255\,000\,000$ RBCs in 500 µL stock

In 180 µL of stock for well ~91 800 000 RBCs

Hemolysis NP : RBC ratio:

20 µL of $(1 \times 10^{13}$ NPs per mL) ~2×10^{11} NPs

$$\Rightarrow (2 \times 10^{11} \text{ NPs})/(91\,800\,000 \text{ RBCs})$$

$$\sim [2178:1]$$

Data availability

Data supporting this article have been included as part of the ESI,† and raw data will be uploaded to FigShare upon acceptance of the article.

Conflicts of interest

CMH and EELT are named as inventors on intellectual property disclosures describing this work.

Acknowledgements

References

1 J. W. Shreffler, J. E. Pullan, K. M. Dailey, S. Mallik and A. E. Brooks, *Int. J. Mol. Sci.*, 2019, **20**, 6056.

2 A. C. Anselmo and S. Mitragotri, *Bioeng. Transl. Med.*, 2019, **4**, 3.

3 M. A. Younis, H. M. Tawfeek, A. A. H. Abdellatif, J. A. Abdel-Aleem and H. Harashima, *Adv. Drug Delivery Rev.*, 2022, **181**, DOI: 10.1016/j.addr.2021.114083.

4 S. Đorđević, M. M. Gonzalez, I. Conejos-Sánchez, B. Carreira, S. Pozzi, R. C. Acúrcio, R. Satchi-Fainaro, H. F. Florindo and M. J. Vicent, *Drug Delivery Transl. Res.*, 2022, **12**, 500–525.

5 E. Udofa and Z. Zhao, *Adv. Drug Delivery Rev.*, 2024, **204**, 115143.

6 L. T. Ferguson, E. D. Hood, T. Shuvaeva, V. V. Shuvaev, M. C. Basil, Z. Wang, J. Nong, X. Ma, J. Wu, J. W. Myerson, O. A. Marcos-Contreras, J. Katzen, J. M. Carl, E. E Morrisey, E. Cantu, C. H. Villa, S. Mitragotri, V. R. Muzykantov and J. S. Brenner, *ACS Nano*, 2022, **16**, 4666–4683.

7 P. M. Glassman, C. H. Villa, O. A. Marcos-Contreras, E. D. Hood, L. R. Walsh, C. F. Greineder, J. W. Myerson, T. Shuvaeva, L. Puentes, J. S. Brenner, D. L. Siegel and V. R. Muzykantov, *Bioconjugate Chem.*, 2022, **33**, 1286–1294.

8 A. C. Anselmo, V. Gupta, B. J. Zern, D. Pan, M. Zakrewsky, V. Muzykantov and S. Mitragotri, *ACS Nano*, 2013, **12**, 11129–11137.

9 J. S. Brenner, S. Mitragotri and V. R. Muzykantov, *Annu. Rev. Biomed. Eng.*, 2021, **23**, 225–248.

10 I. V. Zelepukin, A. V. Yaremenko, V. O. Shipunova, A. V. Babenyshev, I. V. Balalaeva, P. I. Nikitin, S. M. Deyev and M. P. Nikitin, *Nanoscale*, 2019, **11**, 1636.

11 Z. Zhao, A. Ukidve, Y. Gao, J. Kim and S. Mitragotri, *Sci. Adv.*, 2019, **5**, eaax9250.

12 V. Lenders, R. Escudero, X. Koutsoumpou, L. Armengol Álvarez, J. Rozenski, S. J. Soenen, Z. Zhao, S. Mitragotri, P. Baatsen, K. Allegaert, J. Toelen and B. B. Manshian, *J. Nanobiotechnol.*, 2022, **20**, 333.

13 A. M. Curreri, S. Mitragotri and E. E. L. Tanner, *Adv. Sci.*, 2021, **8**, e2004819.

14 E. Beaven, R. Kumar, J. M. An, H. Mendoza, S. C. Sutradhar, W. Choi, M. Narayan, Y. K. Lee and M. Nurunnabi, *Adv. Drug Delivery Rev.*, 2024, **204**, 115157.

15 C. M. Hamadani, G. S. Dasanayake, M. E. Gorniak, M. C. Pride, W. Monroe, C. M. Chism, R. Heintz, E. Jarrett, G. Singh, S. X. Edgecomb and E. E. L. Tanner, *Nat. Protoc.*, 2023, **18**, 2509–2557.

16 G. S. Dasanayake, C. M. Hamadani, G. Singh, S. Kumar Misra, P. Vashisth, J. S. Sharp, L. Adhikari, G. A. Baker and E. E. L. Tanner, *Nanoscale*, 2024, **16**, 5584.

17 G. Singh, G. S. Dasanayake, C. M. Chism, P. Vashisth, A. Kaur, S. K. Misra, J. S. Sharp and E. E. L. Tanner, *Mater. Chem. Front.*, 2023, **7**, 6213.

18 C. M. Hamadani, I. Chandrasiri, M. L. Yaddehige, G. S. Dasanayake, I. Owolabi, A. Flynt, M. Hossain, L. Liberman, T. P. Lodge, T. A. Werfel, D. L. Watkins and E. E. L. Tanner, *Nanoscale*, 2022, **14**, 6021.

19 S. X. Edgecomb, C. M. Hamadani, A. Roberts, G. Taylor, A. Merrell, E. Suh, M. L. Yaddehige, I. Chandrasiri, D. L. Watkins and E. E. L. Tanner, *Electrochem. Sci. Adv.*, 2023, e2300013.

20 C. M. Hamadani, M. J. Goetz, S. Mitragotri and E. E. L. Tanner, *Sci. Adv.*, 2020, **6**, eabd7563.

21 C. M. Hamadani, F. Mahdi, A. Merrell, J. Flanders, R. Cao, P. Vashisth, G. S. Dasanayake, D. S. Darlington, G. Singh, M. C. Pride, W. G. Monroe, G. R. Taylor, A. N. Hunter, G. Roman, J. J. Paris and E. E. L. Tanner, *Adv. Sci.*, 2024, **11**, 2305484.

22 C. M. Hamadani, G. S. Dasanayake, C. M. Chism, M. E. Gorniak, W. G. Monroe, A. Merrell, M. C. Pride, R. Heintz, K. Wong, M. Hossain, G. Taylor, S. X. Edgecomb, D. Jones, J. Dhar, A. Banka, G. Singh, P. Vashisth, J. Randall, D. S. Darlington, J. Everett, E. Jarrett, T. A. Werfel, O. Eniola-Adefeso and E. E. L. Tanner, *Res. Square*, 2023, DOI: 10.21203/rs.3.rs-3146716/v1.

23 J. Zschaler, D. Schlorke and J. Arnhold, *Crit. Rev. Immunol.*, 2014, **34**, 433–454.

24 J. Mestas and C. C. Hughes, *J. Immunol.*, 2004, **172**, 2731–2738.

25 F. Guglietta, M. Behr, G. Falcucci and M. Sbragaglia, *Soft Matter*, 2021, **17**, 5978.

26 D. C. Pan, J. W. Myerson, J. S. Brenner, P. N. Patel, A. C. Anselmo, S. Mitragotri and V. Muzykantov, *Sci. Rep.*, 2018, **8**, 1615.

27 L. Gleue, J. Schupp, N. Zimmer, E. Becker, H. Frey, A. Tuettenberg and M. Helm, *Cells*, 2020, **9**, 2213.

28 A. Benedetto, *Biophys. Rev.*, 2024, **15**, 1909–1939.

29 S. Himbert and M. C. Rheinstädter, *Front. Physiol.*, 2022, **13**, 953257.

30 J. R. Williamson, M. O. Shanahan and R. M. Hochmuth, *Blood*, 1975, **4**, 611–624.

31 Z. Xu, Y. Zheng, X. Wang, N. Shehata, C. Wang and Y. Sun, *Microsyst. Nanoeng.*, 2018, **4**, 17103.

32 E. Kozlova, A. Chernysh, V. Sergunova, E. Manchenko, V. Moroz and A. Kozlov, *In Vitro*, 2019, 8218912.

33 W. Renooij and L. M. G. Van Golde, *FEBS Lett.*, 1976, **71**, DOI: **10.1016/0014-5793(76)80961-1**.

34 J. A. Virtanen, K. H. Cheng and P. Somerharju, *Proc. Natl. Acad. Sci. U. S. A.*, 1998, **95**, 4964–4969.

35 F. Veider, E. Sanchez Armengol and A. Bernkop-Schnürch, *Small*, 2024, **20**, 2304713.

36 A. P. Halestrap and M. C. Wilson, *IUBMB Life*, 2012, **64**, 109–119.

37 K. Geistlinger, J. D. R. Schmidt and E. Beitz, *PNAS Nexus*, 2023, **2**, pgad007.

38 M. L. Jennings, *Am. J. Physiol.: Cell Physiol.*, 2021, **321**, C1028–C1059.

39 M. Glibowicka, B. Winckler, N. Araníbar, M. Schuster, H. Hanssum, H. Rüterjans and H. Passow, *Biochim. Biophys. Acta*, 1988, **946**, 345–358.

40 K. K. Kalsi and J. González-Alonso, *Exp. Physiol.*, 2012, **97**, 419–432.

41 L. Carpenter and A. P. Halestrap, *Biochem. J.*, 1994, **304**, 751–760.

42 M. J. Ovens, A. J. Davies, M. C. Wilson, C. M. Murray and A. P. Halestrap, *Biochem. J.*, 2010, **425**, 523–530.

43 M. J. Capper, S. Yang, A. C. Stone, S. Vatansever, G. Zilberg, Y. K. Mathiharan, R. Habib, K. Hutchinson, Y. Zhao, A. Schlessinger, M. Mezei, R. Osman, B. Zhang and D. Wacker, *Nat. Struct. Mol. Biol.*, 2023, **30**, 1495–1504.

44 M. Hytti, J. Ruuth, I. Kanerva, N. Bhattarai, M. L. Pedersen, C. U. Nielsen and A. Kauppinen, *Mol. Cell. Biochem.*, 2023, **478**, 215–227.

45 S. P. Chai and J. C. Fong, *Cell. Signalling*, 2003, **15**, 269–277.

46 C. Manoharan, M. C. Wilson, R. B. Sessions and A. P. Halestrap, *Mol. Membr. Biol.*, 2006, **23**, 486–498.

47 H. R. Zhekova, J. Jiang, W. Wang, K. Tsirulnikov, G. Kayık, H. M. Khan, R. Azimov, N. Abuladze, L. Kao, D. Newman, S. Y. Noskov, D. P. Tieleman, Z. Hong Zhou, A. Pushkin and I. Kurtz, *Commun. Biol.*, 2022, **5**, 1372.

48 P. Yang, Y. Qin, L. Zeng, Y. He, Y. Xie, X. Cheng, W. Huang and L. Cao, *Biomed. Pharmacother.*, 2023, **165**, 115108.

49 K. Okubo, D. Kang, N. Hamasaki and M. L. Jennings, *J. Biol. Chem.*, 1994, **269**, 1918–1926.

50 J. Y. Xie, J. Ju, P. Zhou, H. Chen, S. C. Wang, K. Wang, T. Wang, X. Z. Chen, Y. C. Chen and K. Wang, *Cell Death Discovery*, 2024, **10**, DOI: **10.1038/s41420-024-01830-w**.

51 J. M. Salhany and L. M. Schopfer, *Blood Cells, Mol., Dis.*, 2001, **27**, 844–849.